Advanced Control Techniques for Post-Buckled Precompressed (PBP) Flight Control Actuators

Mark Groen[a], Michiel van Schravendijk[a], Ron Barrett[b], Roelof Vos[b]
[a]Faculty of Aerospace Engineering, Delft University of Technology, Delft, The Netherlands
[b]Aerospace Engineering Department, The University of Kansas, Lawrence, KS, USA

ABSTRACT

The dynamic response of a new class of flight control actuators that rely on post-buckled precompressed (PBP) piezoelectric elements is investigated. While past research has proven that PBP actuators are capable of generating deflections three times higher than conventional bimorph actuators, this paper quantifies the work output and power consumption under various axial loads, at various frequencies. An analytical model is presented that supports the experimental findings regarding the increasing work output and natural frequency shift under increasing axial loads. Furthermore, increasing axial loads shows an increase in open-loop piezoelectric hysteresis, resulting in an increasing phase lag in actuator response. Current measurements show an electromechanical coupling that leads to power peaks around the natural frequency. Increasing axial loads has no effect on the power consumption, while increasing the work output by a factor of three, which implies a significant increase in work density over the piezoelectric material itself.

Keywords: Post-Buckled Precompressed, PBP, Actuator control, Power consumption, Piezoelectric

NOMENCLATURE

Symbol	Description	Units
b	Actuator width	m
B_a	Distributed coupling stiffness	N
C	Capacitance	F
d	Spring displacement	m
d_{31}	Piezoelectric charge constant	m/V
D_l	Distributed bending stiffness	Nm
E	Young's modulus	N/m^2
E_3	Electric field	V/m
f	Frequency	Hz
F_a	Maximum Axial Force	N
GF	Gauge Factor	-
I	Current	A
k	Spring stiffness	N/m
L	Length	m
m	Mass	kg
P	Electric Power	W
r	Radius of curvature	m
R	Resistance	Ω
t	Thickness, Time	m, sec
u	Displacement	m
U	Normalized displacement	dB
V	Voltage	V
z	Amplification function	-
ε	Strain	-
ζ	Damping ratio	-
θ	End rotation	deg
Θ	Normalized End Rotation	dB
Λ	Actuator Free-Element Strain	-
ν	Poisson's ratio	-
φ	Shape function	m
ω	Angular frequency	rad/s

Active and Passive Smart Structures and Integrated Systems 2009, edited by Mehdi Ahmadian, Mehrdad N. Ghasemi-Nejhad, Proc. of SPIE Vol. 7288, 72881V · © 2009 SPIE · CCC code: 0277-786X/09/$18 · doi: 10.1117/12.816091

Subscripts

a	Actuator
amp	Amplitude
b	Bonding layer
dc	DC offset voltage
e	End cap
n	Natural
p	Piezoelectric element
s	Substrate

1. INTRODUCTION

Fourteen years ago, the first aircraft to use piezoelectric elements for flight control took to the air.[1] The 1.2m wing span aircraft, *Mothra*, flew in September 1994 and demonstrated that fundamental flight control could be achieved by using piezoelectric elements. This was followed by the first rotorcraft, *Gamara*, in December 1996, the first VTOL Micro-Aerial Vehicle (MAV) in September 1997 and a number of missile and munition flight control surfaces through the late 1990's.[2]-[8] These actuators generated significant deflections as seen in Figure 1. In addition to possessing high deflection capability, they also possessed high bandwidth and very low power consumption through the entire speed range.

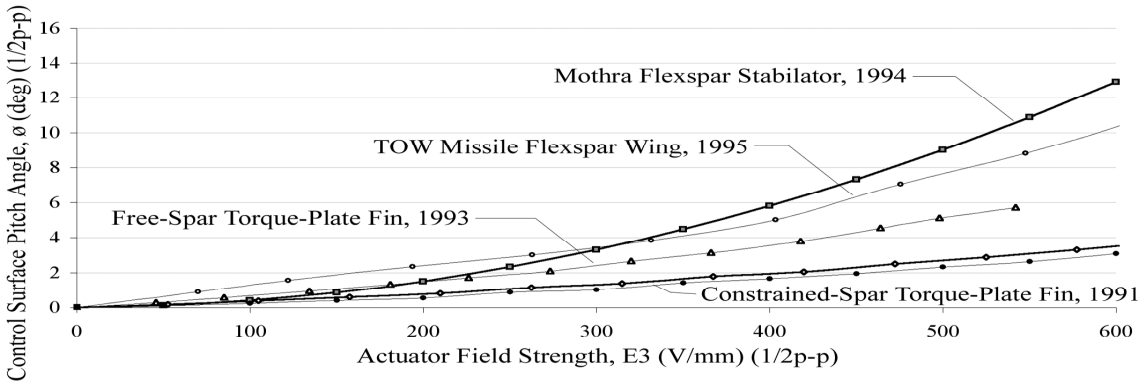

Figure 1. Quasi-Static Half-Peak Control Surface Deflection with Actuator Field Strength[1]-[8]

Although these flight control systems worked well, they employed piezoceramic actuators which experienced a linear decay in moment and force generation capability with increasing deflections. Because the flight control systems were both aerodynamically and inertially balanced, no flutter tendencies were ever observed in any wind tunnel or flight test.[8] However, their "soft spring" deflection properties at the limits of their stroke meant that buffet and stall loads simply could not be resisted. Figure 2 shows the typical actuator moment generation decay with increasing deflection which is a hallmark of early piezoceramic actuator elements.

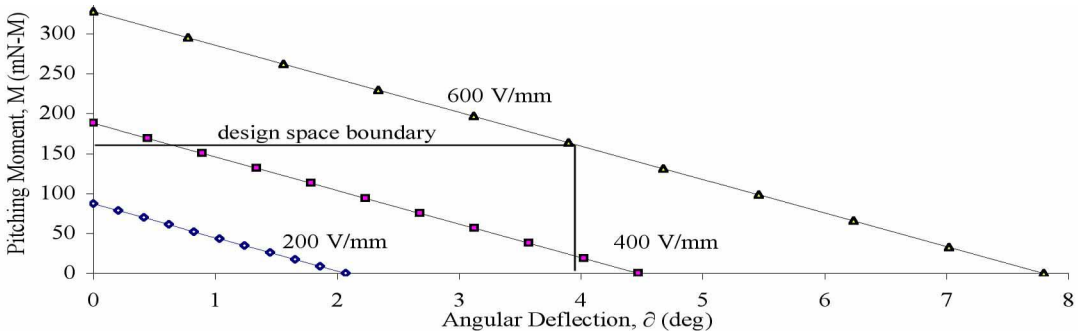

Figure 2. Typical Pitching Moment Versus Angular Deflection Design Space Relationship for Piezoceramic Actuators[8]

From Figure 2 it can be seen that the design space boundary which is typically laid out by aeromechanicians is completely enclosed within the maximum field lines of the actuator itself with the knee of the design space boundary hitting the mid-point. Typically, designers chose this point as it maximizes the amount of work which can be obtained from a given volume, mass or unit cost of piezoceramic actuator element. Still, there are serious design challenges, for instance, half of the deflection and moment generation capability of the actuator goes essentially unused. Also, at high strokes, moment capability is limited which retards the ability of a flight control surface to fight overdesign aeroloads. With proper configuration design, the stall rotations could actually maximize deep stall stability. Still, susceptibility to buffet deflections meant that gust fields would typically induce uncommanded rotations. To retard this, designers were faced with the unpalletable choice of increasing the actuator weight and volume by as much as an order of magnitude.

Fortunately, in recent years a new branch of piezoceramic actuation has evolved from its beginnings as electrical transducers. In the late 1990's a discovery was made that enabled the apparent piezoelectric coupling coefficients to be increased dramatically.[9]-[10] Although only tangentially related to flight control, this basic discovery ushered in a new era in the control of structures with piezoelectric elements. Because it was found that by applying axial forces to a bender element, the deflections could be increased dramatically, the move beyond electrical transduction was natural. The first applications involved advanced flight control actuators being used in high performance convertible UAVs, missiles and munitions.[11]-[17]

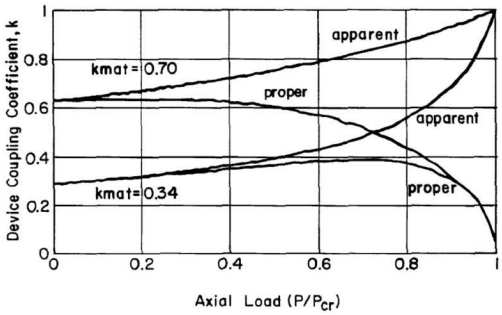

Figure 3. Fundamental PBP Actuator Layout and Dramatic Increase in Coupling Coefficient[10]

The advantages of this form of actuation were clear: *much higher deflection with no reduction in moment generation capability*. For the first time in the piezoceramic actuation world, the designer no longer would have to compromise moment generation capability at higher deflections -- both could be obtained simultaneously. Clearly, the dramatically increased coupling coefficients observed in transducer experiments were being replicated in flight control devices.

The advantages of PBP actuation were numerous and included high performance for negligible weight, volume and cost increments. However, one serious problem was introduced which needed to be dealt with: tensile failure on the convex face of the actuator. To retard this, a system which actively shifts the elastic axis through the thickness of the element, was conceived.[14]-[18] This Dynamic Elastic Axis Shifting (DEAS) lent a high degree of protection to the PBP system as it placed all elements in the actuator in compression at all times. By doing so, tensile failure modes disappeared.

Although the actuators work well, significant reductions in driven natural frequencies have been observed. Because moment generation capability of properly designed and tuned PBP elements is not significantly reduced throughout the deflection envelope and mass additions are very small, the commanded speeds should be comparable or superior to conventional piezoceramic actuators. Because the PBP elements are fundamentally capable of generating higher deflections and moments simultaneously, and therefore doing more total work for the same amount of piezoceramic, they are also capable of absorbing more total electrical energy. Accordingly, this study is the first to specifically quantify these nonlinear effects so as to aid the flight control system designer in properly laying out electrical driving networks for PBP actuators.

2. ANALYTICAL MODEL

In an attempt to predict the dynamic behavior of a PBP actuator, the actuator is modeled using Euler-Bernoulli beam theory. The displacement $u(x,t)$ of the actuator is substituted by the product of a shape function, $\varphi(x)$ and an amplification function of time, $z(t)$:[19]

$$u(x,t) = \varphi(x) z(t) \tag{1}$$

Using a virtual work approach, the equation of motion for the axially loaded PBP actuator can be expressed as:

$$\left[m \int_o^L \varphi^2 dx \right] \ddot{z} + \left[\int_o^L \left(D_l (\varphi'')^2 - \frac{F_a}{b} (\varphi')^2 \right) dx \right] z = \Lambda_1(t) \left[\int_o^L \varphi'' dx \right] \tag{2}$$

If one considers a linear relationship between applied field and free-element strain, Λ_1, in the in-plane (1) direction Equation 2 can be slightly simplified:

$$\left[m\int_o^L \varphi^2 dx \right]\ddot{z} + \left[\int_o^L \left(D_l(\varphi'')^2 - \frac{F_a}{b}(\varphi')^2 \right) dx \right] z = B_a d_{31} E_3(t) \left[\int_o^L \varphi'' dx \right] \tag{3}$$

In this model the PBP actuator is loaded by a constant axial force F_a and as a forcing function the applied electrical field in the thickness direction E_3 is multiplied with the piezoelectric charge constant d_{31}. Damping depends on many (non)-linear factors and has been neglected in this model. Furthermore, given that a uniform beam is considered, the mass per unit length per unit width m is defined as:

$$m = 2\rho_p t_p + 2\rho_b t_b + \rho_s t_s \tag{4}$$

The stiffness properties of PBP actuators are modeled with classical laminated plate theory.[20]-[21] For a conventional bimorph actuator element this results in the following bending stiffness coefficient, D_l, and coupling stiffness coefficient, B_a:

$$D_l = E_s \frac{1}{1-\nu_s^2}\frac{t_s^3}{12} + E_p \frac{1}{1-\nu_p^2}\left[\frac{1}{2}(t_s + 2t_b)^2 t_p + (t_s + 2t_b)t_p^2 + \frac{2}{3}t_p^3 \right] \tag{5}$$

$$B_a = E_p \frac{1+\nu_p}{1-\nu_p^2}\left(t_s t_p + 2t_b t_p + t_p^2 \right) \tag{6}$$

The material properties and dimensions that appear in Equations 5 and 6 can be found in Figure 5 and Table 1 of Section 3. A sinusoidal function, $\varphi(x)$, is chosen to approximate the shape of the actuator element:

$$\varphi(x) = \sin(\pi x / L) \tag{7}$$

The single sine function complying with pinned-pinned boundary conditions can be shown to approximate the shape of the actuator element within 4 % accuracy.[15] Using the software package MATLAB to solve Equation 3, an amplitude response can be found. Figure 4 shows the amplitude response as function of the frequency of the harmonic forcing function, where U is the amplitude, normalized with respect to the amplitude of the uncompressed (F_a = 0) response at f = 0.1Hz.

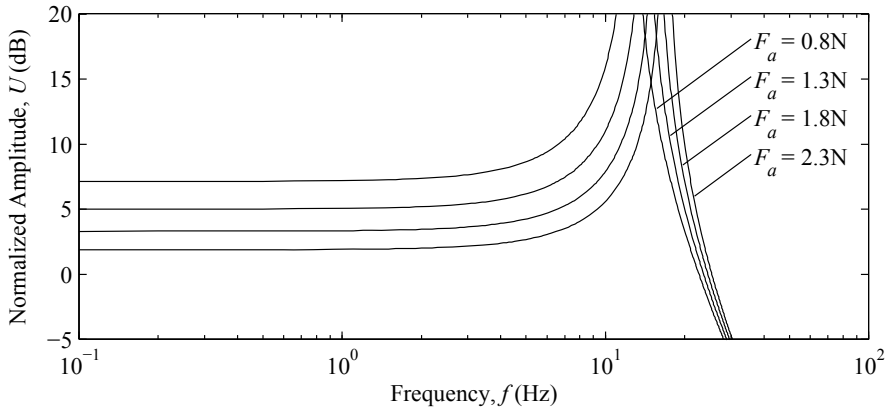

Figure 4. Bode amplitude plot normalized to uncompressed response at 0.1Hz

From Figure 4 it can be seen that the model predicts an amplitude-response growth for increasing axial force while the natural frequency decreases with increasing axial force. Furthermore it can be seen that the amplitude response extends to infinity in this model, since damping has been neglected.

3. EXPERIMENTAL SETUP AND DATA ACQUISITION

3.1 Actuator Design and Fabrication

To characterize the dynamic behavior of a PBP actuator, a test setup was built. To make sure the natural frequency was in the low frequency range (<50Hz), a 230mm long and 11.2mm wide specimen was used. The actuator was made using an aluminum substrate with on either side 3 PZT elements along the length of the substrate, see Figure 5. To transfer bending stresses from one element to another, glass-fiber strips were applied on the seams between the elements. The bonding layer consisted of Hysol 9412. A schematic overview of the actuator layup and dimensions is given in Figure 5 and properties and dimensions of the materials are given in Table 1.

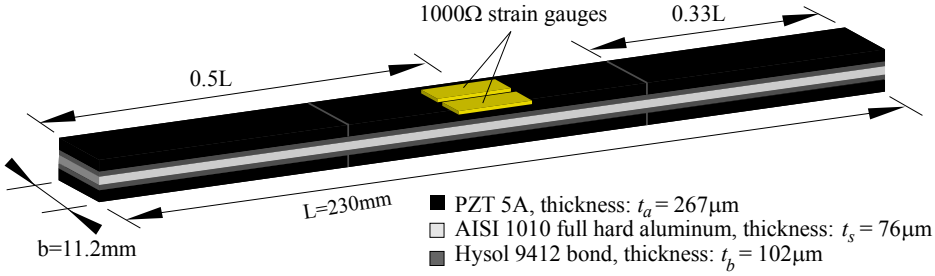

Figure 5. Schematic overview of the PBP actuator and the Wheatstone bridge

The strain due to the bending of the actuator was measured by two strain gauges placed at the center of the PBP actuator on either side of the actuator. The 1000Ω strain gauges were connected in a full Wheatstone bridge configuration to get a maximum resolution.

Table 1. Properties and dimensions of actuator

	Piezo element	Substrate	Bond Line
Material	PZT 5A	AL 1100-H18	Hysol 9412
Thickness, t	267 μm	76 μm	102 μm
Density, ρ	7800 kg/m^3	2700 kg/m^3	2400 kg/m^3
Stiffness, E	61 GPa	70 GPa	1 GPa
Poisson's ratio, v	0.31	0.3	0.3

During the experiment the actuator was placed vertically in an Instron tensile test machine. The actuator was pinned on either side to provide free rotation, while on the on the bottom side the pinned specimen was connected to a compression spring with spring stiffness k. The axial force could be set by adjusting the height, d between the clamps on the Instron (see Figure 6). The force transducer of the tensile test machine provided an accurate measurement up to 1mN of the applied axial force on the specimen.

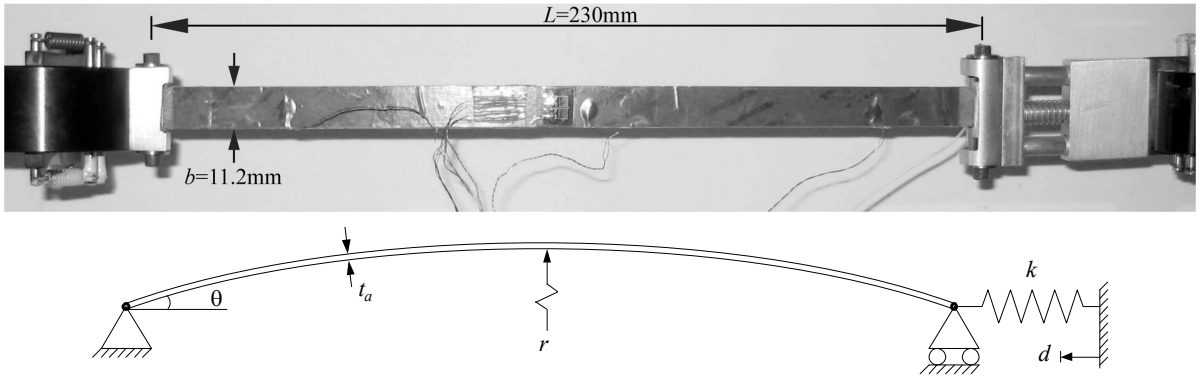

Figure 6. Front view photo and schematic side view of the setup

3.2 Data Acquisition and Processing

The data acquisition and actuator control was done with a data acquisitioning device (DAQ). This device was controlled by the software package LabVIEW of National Instruments. The DAQ measured the dynamic response of the actuator, by means of the differential voltage ΔV from the Wheatstone bridge, as well as the current supplied to the actuator. The DAQ was also used for the 5V power supply to the Wheatstone bridge. The low-voltage actuator control signal coming from the DAQ was amplified to supply the actuator with a signal of the form Equation 8, where the V_{dc} is a DC offset voltage, V_{amp} the amplitude of the signal and f the frequency in Hz:

$$V(t) = V_{dc} + V_{amp} \sin(2\pi f t) \tag{8}$$

The acquired data was processed in MATLAB with a least square method to determine the amplitude of the sinusoidal actuator response and the amplitude of the sinusoidal current signal. The strain at the midpoint of the actuator was calculated by relating the differential voltage ΔV to the differential resistance in a strain gauge, ΔR:

$$\frac{V_{wb} + \Delta V}{2V_{wb}} = \frac{R_{sg} + \Delta R}{2R_{sg}} \tag{9}$$

Where V_{wb} is the voltage over the Wheatstone bridge, 5V and R_{sg} is the resistance of a strain gauge, 1000Ω. Knowing the gauge factor, GF was 2.09, the strain was calculated according to:

$$\varepsilon = \frac{\Delta R}{GF \cdot R_{sg}} \tag{10}$$

To calculate the end rotation of the actuator, only first mode circular bending was assumed. Furthermore it was assumed that the neutral line of the actuator coincided with the central line of the actuator, so that the strain on each side of the actuator was constant and opposite. From Figure 6 the following relation can be derived assuming a circular arc shape function:

$$\frac{\theta\left(r + \frac{t_a}{2}\right)}{\theta r} = \frac{L + \Delta L}{L} \tag{11}$$

Knowing that the strain is defined as the differential length ΔL divided by the total length L, the end rotation, θ, was calculated by:

$$\theta = \frac{L}{2r} = \frac{L}{t_a}\varepsilon \tag{12}$$

Calibration at low frequency with laser reflection techniques, showed the end rotation to correspond, to the calibrated rotation within 10 percent. Furthermore the end rotation in the measurements was corrected for an offset in strain. This offset was introduced in the strain gauges by the axial force and by imperfections in the actuator. In addition, the actuator supply signal was given a DC offset voltage, V_{dc} such that the actuator showed symmetrical bending around a straight position. This was determined by measuring the axial force. Since the axial force was related to the vertical displacement of the actuator tip, a straight position of the actuator lead to the maximum axial force. While supplying a sinusoidal voltage to the PBP actuator with forcing frequency, f, the axial force showed a sinusoidal behavior with twice the forcing frequency. For each set of measurements the Instron clamps were given a certain displacement, d. This resulted in a maximum axial force:

$$F_a = k \cdot d \tag{13}$$

The axial force levels, F_a chosen for the experiment were: 0.8N, 1.3N, 1.8N and 2.3N. The maximum applied axial force was set to be 2.3N, because when applying axial loads higher than 2.6N the actuator began to exhibit snap-trough behavior which is not the subject of this study.[22]

4. RESULTS

To be able to make a suitable control system for a PBP actuator it is important to have a good understanding of the actuator response over the complete frequency range. This response was measured by supplying the actuator with a sinusoidal signal and measuring the response of the actuator during a frequency sweep from 0.1 to 100 Hz. This was done for a supply voltage of different amplitudes as well as for different axial loads. Beside the actuator response, the supply voltage and current were also measured, such that the power consumption with frequency could be determined.

4.1 The Quasi-static Response of the PBP Actuator

When considering the low frequency response ($f < 0.1f_n$), the actuator response is assumed to be quasi-static. Using the average time response for frequencies between 0.1Hz and 1.0Hz the quasi-static response of the PBP actuator was measured for various axial loads and supply voltages. Figure 7 shows the results for the end rotation, θ, as a function of axial load for different supply voltages.

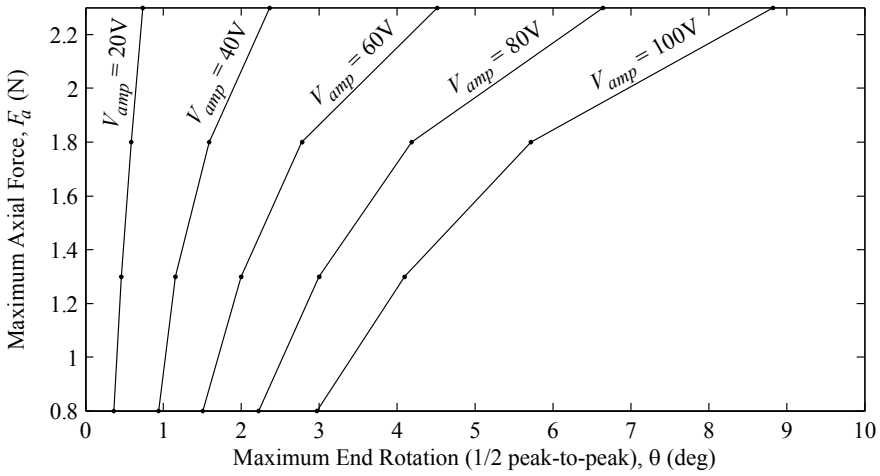

Figure 7. Quasi-static actuator response

From Figure 7 it can be seen that end rotations grow exponentially when an axial force is applied. For example, by applying a maximum axial force of 2.3N to the actuator, the maximum end rotation of the actuator shows an increase of a factor 3 when applying a 100V supply voltage.

4.2 The Dynamic Response of the PBP Actuator

The dynamic response of the actuator was determined by applying the supply signal as given in Equation 8, for frequencies ranging from 0.1Hz to 100Hz and for various axial loads.

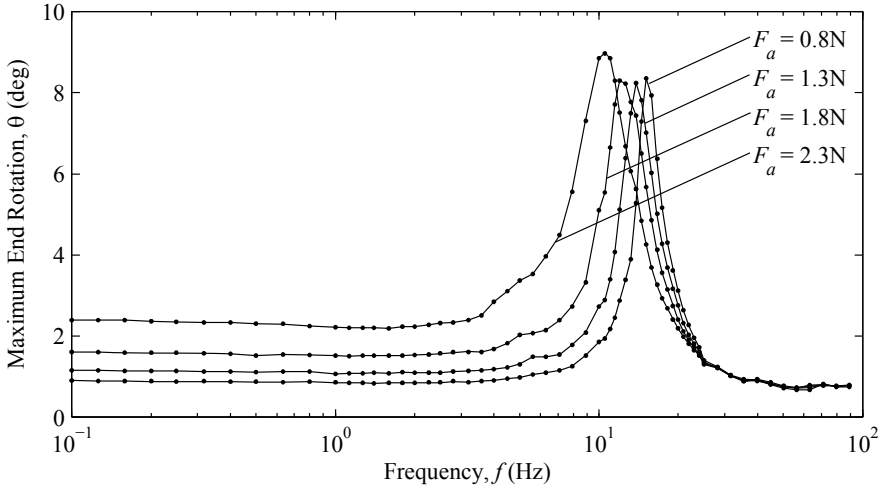

Figure 8. The Bode amplitude plot for a sinusoidal supply between 40V and -40V

Figure 8 shows the Bode amplitude plot for a supply voltage with V_{amp} = 40V and V_{dc} = 0V. Similar to the quasi-static case, it can be seen that an increase in applied axial force led to an increase in end rotation up until the resonance frequency was reached. In addition Figure 8 shows the amplitude response peaks at the natural frequency. Just as the analytical model predicted, the natural frequency decreased with an increasing axial force. This feature can be seen more clearly when the actuator response is normalized with respect to the quasi-static response and is plotted in decibels (see Figure 9).

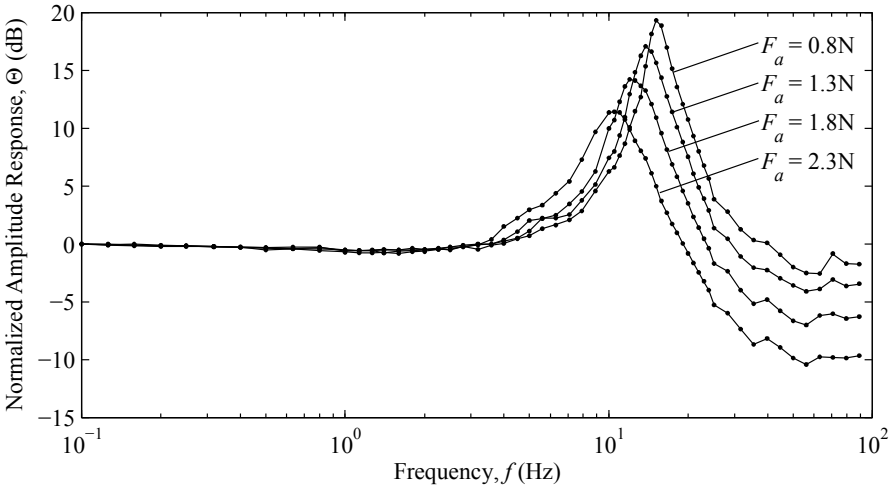

Figure 9. The Bode amplitude plot for a sinusoidal supply between 40V and -40V with normalized amplitude response

It can be seen that with increasing axial force also the damping ratio increased. To get values for the natural frequency and damping ratio the experimental results were compared to a second order model, see Equation 14.

$$\frac{d^2x}{dt^2} + 2\zeta\omega_n \frac{dx}{dt} + \omega_n{}^2 = 0 \tag{14}$$

Equation 14 is the differential equation belonging to a second order system with ω_n the natural frequency and ζ the damping ratio. The experimental resonance peaks were matched with resonance peaks of the second order system and the results are listed in Table 2.

Table 2. Measured and analytical natural frequencies

	Measured ω_n	Measured ζ	Analytical ω_n (Eq.3)
F_a = 0.8N	15.2 Hz	0.05	17.0 Hz
F_a = 1.3N	13.8 Hz	0.07	15.6 Hz
F_a = 1.8N	12.5 Hz	0.10	14.2 Hz
F_a = 2.3N	10.6 Hz	0.13	12.5 Hz

Even though there was an offset of about 2Hz between the analytically predicted and measured natural frequency, the trend in natural frequency decay was properly captured by the analytical model. The offset could be explained by the fact that the material properties in the analytical model are assumed constant over the length of the element, while in reality the actuator properties varied along the length due to manufacturing imperfections. The stiffness and density at the seams between the individual PZT sheets changed, which could have led to the small mismatch between theory and experiment in Table 2. The damping in the actuator depended on many (nonlinear) features such as friction in the hinges and structural damping and was neglected in the analytical model.

4.3 Hysteresis within the PBP Actuator

Along with the Bode amplitude plots also Bode phase plots were made. Figure 10 shows the phase plot for a supply voltage with V_{amp} = 40V en V_{dc} = 0V. It can be seen that the actuator shows second-order system behavior with a phase

shift of 180 degrees beyond the natural frequency. In contrast to a second-order system, at low frequencies there is already some initial phase lag present in the actuator. This phase lag is attributed to hysteresis in the piezoelectric elements.

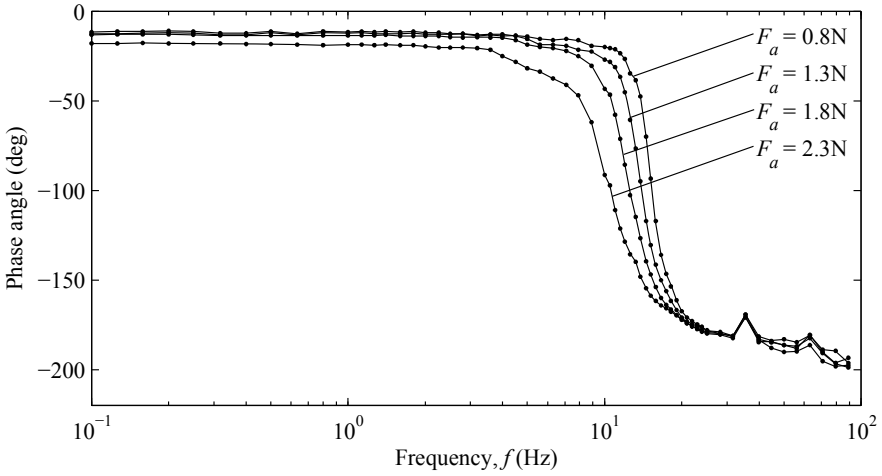

Figure 10. The Bode phase plot for a sinusoidal supply between 40V and -40V

To examine the hysteresis of the actuator, Figure 11 shows the quasi-static response of the actuator averaged over 20 cycles for a maximum axial force, F_a=1.3N. It can be seen that the area and the shape of the hysteresis cycle changes with the control signal parameters V_{amp} and V_{dc}, see Equation 8.

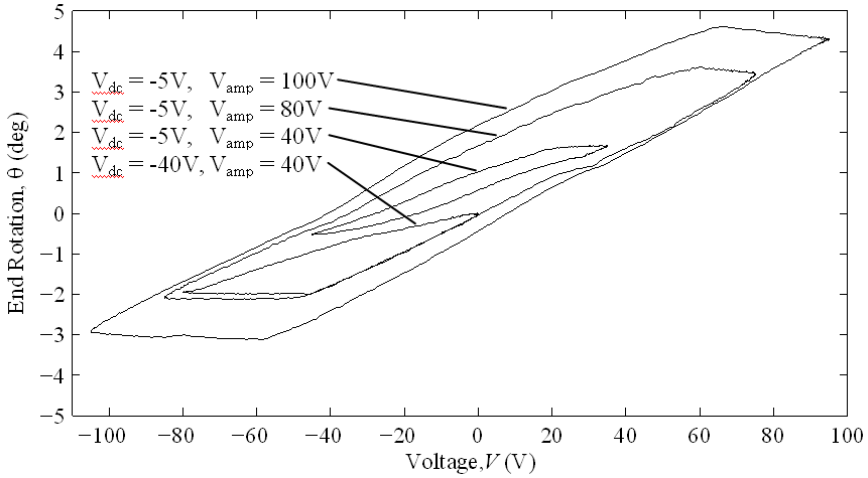

Figure 11. Hysteresis cycles of the PBP actuator for a maximum axial force, F_a= 1.3N

The area and shape of the hysteresis also changes with increasing axial force. From Figure 12 it can be seen that the hysteresis of a cycle grows with increasing axial force. Calculating the hysteresis by dividing the area swept within the hysteresis loop by the area of the peak rotation-voltage box, gave an increase in hysteresis from 17 percent to 27 percent by applying a maximum axial force, F_a, of 0.8N to respectively 2.3N.

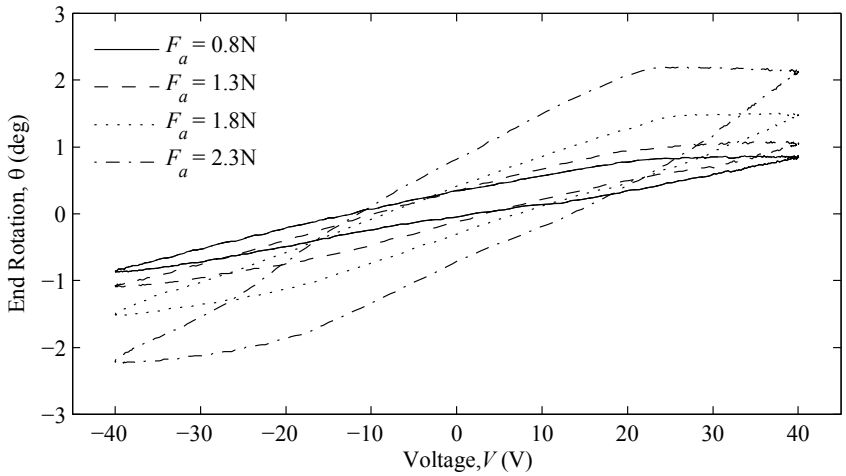

Figure 12. Hysteresis cycles of the PBP actuator for a sinusoidal supply between 40V and -40V

4.4 Power Consumption of the PBP Actuator

Beside the actuator response, also the current to the actuator was measured. This was done by measuring the voltage over a 100Ω resistor mounted in the supply circuit. The voltage over this resistor stayed below 1 percent of the supply voltage for the most interesting frequency range (<35Hz), so this was considered not to affect the actuator response. The measured current (one half peak-to-peak) increased linearly with increasing frequency, which resulted in an exponential curve on the log-scale as seen in Figure 13.

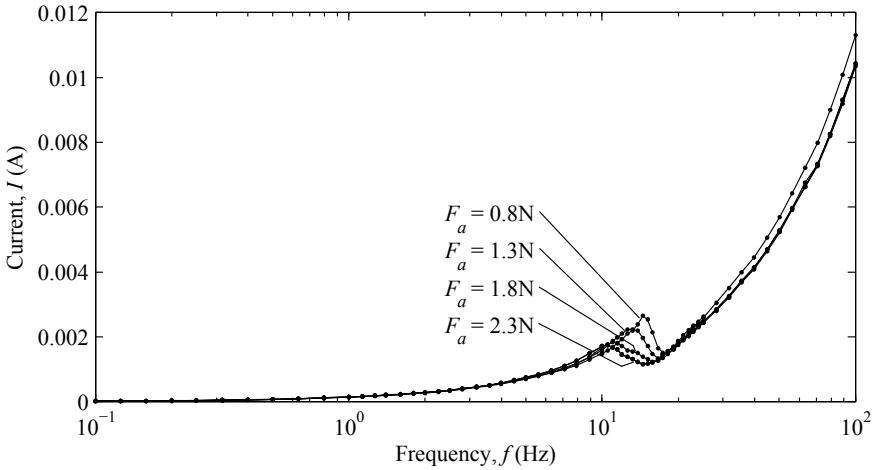

Figure 13. The measured current amplitude for a sinusoidal supply between 40V and -40V

In Figure 13 the resonance peak at the natural frequency can be seen to induce a current peak, which clearly indicates an electro-mechanical coupling in the PBP actuator. The current appeared to be the same when different axial forces were applied, except near the resonance peak where the height and frequency of the current peak changed with axial load. For a regular dielectric material the current is proportional to a constant capacitance C times the time derivative of the voltage:

$$I(t) = C\frac{dV}{dt} \tag{15}$$

Using Equation 15 to calculate the capacitance of the actuator, the coupling between capacitance and dynamic response could be demonstrated. In Figure 14 the effective electrodynamic capacitance of the actuator was calculated with the current response for a supply signal with V_{amp} = 20V and an axial force of F_a = 1.3N. The capacitance was compared to that of an unconstrained single sheet of PZT-5A, depicted as the reference response in Figure 14.

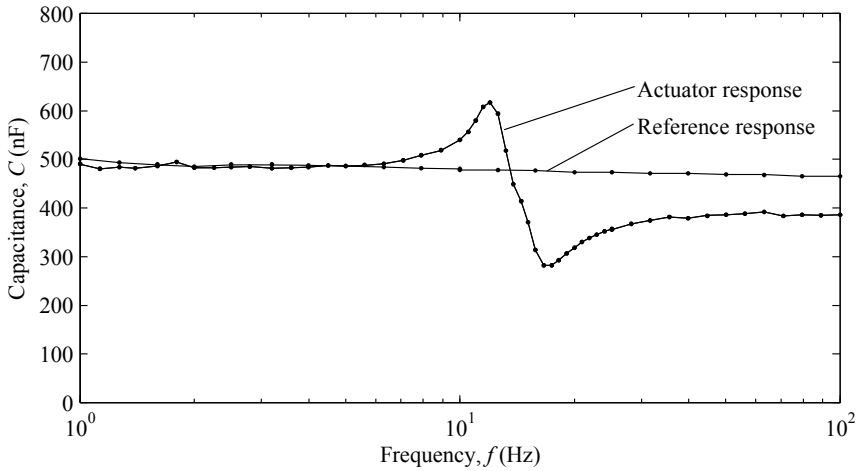

Figure 14. Effective electrodynamic capacitance of the of the PBP actuator as calculated with the response for a sinusoidal supply between 20V and -20V

In accordance to earlier research the capacitance showed a resonance peak followed by an anti-resonance peak at the natural frequency.[22] The 180 degree phase lag between the actuator motion and the supply voltage lowers the capacitance of the actuator for frequencies beyond the natural frequency.

Multiplying the voltage and current at every time instant and taking the average, resulted in the average or real power consumption by the actuator. In Figure 15 the power consumption is shown for V_{amp} = 40V.

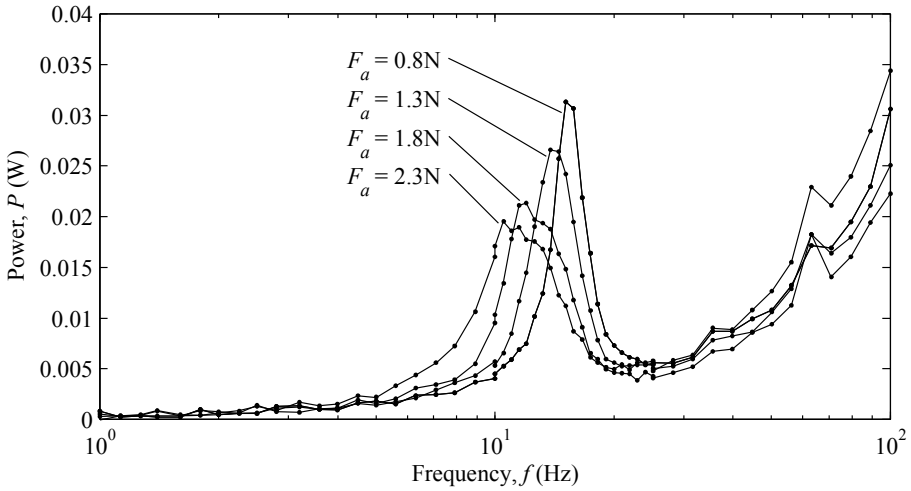

Figure 15. The applied electrical power to the actuator for a sinusoidal supply between 40V and -40V

From Figure 15 it can be seen that the power consumption increases with increasing frequency and is for all axial forces roughly the same, except near the natural frequency where the power consumption peaks. The phase angle between the voltage and current also showed a slow decrease with increasing frequency from 86 to 80 degrees, except again near the natural frequency where the phase angle dropped to 45 degrees. In this experiment the actuator was unloaded, but for this condition the power input for low frequencies remained the same, while the work output increased by a factor of three. So there was a significant increase in efficiency, when applying an axial force.

5. CONCLUSIONS

This study examined the relationship between the driving electrical signals of PBP elements and their observed electrical and mechanical properties. Bench tests on a uniform 230mm long PZT-5A and aluminum PBP actuator showed that increasing axial forces led to up to a factor of three higher deflections. The natural frequency decreased from 15.2Hz to 10.6Hz with increasing axial loads, while the damping ratio was shown to increase from 0.05 to 0.13. An analytical

model based on a single sinusoidal mode shape was developed and showed good correlation to the experimentally obtained natural frequencies. Furthermore, it was shown that with increasing axial loads the observed hysteresis grew from 17 to 27 percent, resulting in an increasing phase lag in actuator response. In addition, electromechanical coupling was observed that led to a resonance and anti-resonance peak in the effective electrodynamic capacitance of the actuator. This resulted to power peaks around the natural frequency. Increasing axial loads had no effect on the gross power consumption. This of course, implies a significant increase in transfer efficiency over a wide range of frequencies due to the application of an axial force.

REFERENCES

[1] Barrett, R., "All-Moving Active Aerodynamic Surface Research," Journal of Smart Materials and Structures, Vol. 4(4), 65-74 (1995)

[2] Barrett, R., and Howard, N., "Adaptive Aerostructures for Subscale Aircraft," refereed proceedings of the 20th Southeastern Conference on Theoretical and Applied Mechanics," Pine Mountain, GA, (2000)

[3] Barrett, R., and Frye, P., and Schliesman, M., "Design, Construction and Characterization of a Flightworthy Piezoelectric Solid State Adaptive Rotor," Journal of Smart Materials and Structures, Vol. 7(3), 422-431 (1998)

[4] Barrett, R. and Stutts, J., "Design and Testing of a 1/12th Scale Solid State Adaptive Rotor," Journal of Smart Materials and Structures, Vol. 6(4), 491-497 (1997)

[5] Barrett, R., "Active Aeroelastic Tailoring of an Adaptive Flexspar Stabilator," Journal of Smart Materials and Structures, Vol. 5(6), 723-730 (1996)

[6] Barrett, R. and Brozoski, F., "Missile Flight Control using Active Flexspar Actuators," Journal of Smart Materials and Structures, Vol. 5(2), 121 – 128 (1996)

[7] Barrett, R., "Adaptive Aerostructures, Improving High Performance, Subcale Military UAVs," proc. AIAA paper 2004-1886 (2004)

[8] Barrett, R., "Adaptive aerostructures: the first decade of flight on uninhabited aerial vehicles," proc. SPIE Paper 5388-19 (2004)

[9] Lesieutre, G.A., and C.L. Davis, "Can a Coupling Coefficient of a Piezoelectric Actuator be Higher Than Those of Its Active Material?," Journal of Intelligent Materials Systems and Structures, Vol. 8, 859-867 (1997)

[10] Lesieutre, G. A. and Davis, C. L., "Transfer Having a Coupling Coefficient Higher than its Active Material," US Pat. 6,236,143 issued 22 May 2001

[11] Vos, R., Barrett, R., Van Tooren, M. and Krakers, L., "Post-Buckled Precompressed (PBP) Piezoelectric Actuators for UAV Flight Control," proc. SPIE Paper 6173-15 (2006)

[12] De Breuker, R., Tiso, P., Vos, R. and Barrett, R., "Nonlinear Semi-Analytical Modeling of Post-Buckled Precompressed (PBP) Piezoelectric Actuators for UAV Flight Control," Proc. AIAA Paper AIAA-2006-1795 (2006)

[13] Barrett, R., McMurtry, R., Vos, R., Tiso, P. and De Breuker, R., "Post-Buckled Precompressed Piezoelectric Flight Control Actuator Design, Development and Demonstration," Journal of Smart Materials and Structures, Vol. 15(5), 1323-1331 (2006)

[14] Barrett, R. and P. Tiso, "PBP Adaptive Actuator Device and Embodiments," International Patent Application number PCT/NL2005/000054, via Technische Universiteit Delft, The Netherlands

[15] Vos, R., De Breuker, R., Barrett, R. and Tiso, P.,"Morphing Wing Flight Control Via Postbuckled Precompressed Piezoelectric Actuators," Journal of Aircraft, Vol. 4(4), 1060-1068 (2007)

[16] Vos, R., Barrett, R., De Breuker, R. and Tiso, P., "Post-Buckled Precompressed Elements: A New Class of Control Actuators for Morphing Wing UAVs," Journal of Smart Materials and Structures, Vol. 16(3), 919-926 (2007)

[17] Barrett, R. and Vos, R., "Post-Buckled Precompressed (PBP) Subsonic Micro Flight Control Actuators and Surfaces," proc. SPIE paper 6525-21 (2007)

[18] Vos, R. and Barrett, R., "Dynamic Elastic Axis Shifting: An Important Enhancement of Postbuckled Precompressed (PBP) Actuators," proc. AIAA paper AIAA-2007-1705 (2007)

[19] Thomson, W. T. and Daleh, M. D., [Theory of Vibrations with Applications], Prentice hall, New Jersey (1998).

[20] Barrett, R., "Active Plate and wing research using EDAP elements," Journal of Smart Materials and Structures, Vol.1, 214-226 (1992).

[21] Jones, R., [Mechanics of Composite Materials], Hemisphere Publishing Cooperation, New York, Chapter 3 (1975).

[22] Giannopoulos, G., [Large Displacement Piezoelectric Structures for Actuation Applications], Dissertation, Vrije Universiteit Brussel, Brussels (2007)